Progress In Electromagnetics Research B, Vol. 118, 56–71, 2026

(Received 11 June 2026, Accepted 19 July 2026, Scheduled 29 July 2026)

Software-Validated Computational Framework for Axial and Radial Magnetic Force Prediction in Misaligned Air-Core Coil Systems with Surrogate Modeling

Ali Jebelli[1,*], Nafiseh Lotfi[2], Arezoo Mahabadi[3], and Mustapha C. E. Yagoub[4]

[1] *College of Business, Engineering and Technology, Kentucky State University, Kentucky, USA*
[2] *Department of Engineering and Design, Robotic Century, Kentucky, USA*
[3] *Department of Engineering and Design, Robotic Century, Alberta, Canada*
[4] *School of Electrical Engineering and Computer Science, University of Ottawa, Ontario, Canada*

ABSTRACT: Accurate prediction of magnetic forces in air-core coil systems is essential for the design and optimization of electromagnetic actuators, wireless power transfer systems, inductive coupling devices, and precision electromagnetic assemblies. This paper presents a software-validated computational framework for predicting axial and radial magnetic forces in practical air-core coil systems under aligned and misaligned conditions. The proposed framework extends classical coaxial coil-force theory by incorporating lateral offset, angular tilt, finite coil dimensions, discrete winding geometry, helical winding pitch, finite conductor diameter, and realistic conductor placement. Three complementary physics-based methods are developed: a semi-analytical elliptic-integral method for fast coaxial evaluation, a direct numerical-integration method based on the Lorentz-force formulation, and a filament-based discrete-winding model for realistic conductor representation. Independent Ansys Maxwell finite-element simulations are used as the software-validation reference under identical geometric and electrical conditions. This study is limited to software-based validation, while experimental verification is identified as future work. The results show strong agreement among all methods and the finite-element reference. Mesh-independence and boundary-domain tests confirm numerical stability, with final variations of 0.15% and 0.12%, respectively. The maximum axial-force deviation is 0.62%, while the radial-force symmetry error remains below 0.23%. Incorporating practical winding details reduces the model-to-software error from 2.87% to 0.10%. A feedforward neural-network surrogate model trained on 12,000 validated samples achieves $R^2 = 0.996$–0.998, with mean relative error below 1.20% and maximum error of 5.00%. The proposed framework provides an accurate, efficient, and physically consistent tool for force prediction and design optimization in practical coil systems.

1. INTRODUCTION

Magnetic forces generated by current-carrying coils are fundamental in a wide range of electromagnetic and electromechanical systems, including electromagnetic actuators, wireless power transfer systems, inductive coupling devices, precision positioning platforms, magnetic levitation systems, and superconducting coil assemblies [1–6]. Accurate prediction of coil-coil interaction forces is essential because these forces directly influence system stability, actuation efficiency, alignment sensitivity, vibration behavior, and overall electromagnetic performance. While axial force under ideal coaxial alignment is often the primary design parameter, practical coil systems frequently experience radial and tangential force components due to lateral offset, angular misalignment, and manufacturing tolerances. Therefore, a general computational framework capable of predicting both axial and radial magnetic forces under realistic conditions is required.

Classical electromagnetic theory provides the foundation for magnetic-force modeling through the Biot-Savart law, Lorentz force formulation, Maxwell mutual-inductance theory, and magnetic co-energy principles [1–4, 11]. For ideal coaxial circular coils, analytical and semi-analytical formulations based on elliptic integrals provide efficient and accurate force evaluation [1–3, 7–13]. However, these classical models rely on simplifying assumptions such as perfect coaxial alignment, continuous current distribution, negligible winding pitch, and idealized conductor geometry. These assumptions limit their applicability to practical wound coils where discrete turns, finite conductor diameter, insulation spacing, and helical winding geometry significantly affect magnetic-force behavior.

To overcome these limitations, several numerical and semi-analytical methods have been developed, including mutual-inductance-based formulations, filament discretization techniques, and spatial field computation methods [14–16, 19]. Finite-element electromagnetic simulation tools such as Ansys Maxwell provide highly accurate solutions but are computationally expensive for repeated evaluation, parametric studies, and optimization processes [22]. Therefore, there is a need for efficient physics-based models that preserve accuracy while significantly reducing computational cost.

Recent advances in machine learning have introduced surrogate modeling techniques for electromagnetic systems, en-

* Corresponding author: Ali Jebelli (ali.jebelli@kysu.edu).

abling rapid prediction of fields, inductances, and forces once trained on validated datasets [17, 18, 21]. However, such data-driven models must remain physically consistent and restricted to validated parameter domains to avoid unreliable extrapolation.

Several studies by Jebelli et al. have developed analytical and numerical models for axial magnetic-force prediction in coaxial air-core coil systems [23–25]. While these works provide important benchmarks for ideal coaxial configurations, practical systems require a more general framework that includes radial force prediction, angular misalignment, and realistic winding representation.

Motivated by these challenges, this paper presents a software-validated computational framework for predicting axial and radial magnetic forces in misaligned air-core coil systems. The proposed framework integrates three complementary physics-based methods: a semi-analytical elliptic-integral formulation, a direct numerical-integration method based on the Lorentz-force law, and a filament-based discrete-winding model capable of representing realistic conductor geometry, including helical pitch and finite conductor size. These methods are systematically validated against independent Ansys Maxwell finite-element simulations under identical geometric and electrical conditions [22].

In addition, a feedforward neural-network surrogate model is developed and trained using validated simulation data to enable rapid force prediction and design-space exploration. The surrogate model is restricted to interpolation within the validated domain and is not used for extrapolation beyond trained conditions.

The main contribution of this work is not the individual application of classical electromagnetic theory or machine learning, but rather the integration of analytical, numerical, filament-based, finite-element software validation, and surrogate modeling into a unified and reproducible framework for axial and radial force prediction in practical misaligned air-core coil systems. The framework explicitly accounts for lateral offset, angular tilt, radial and tangential force decomposition, practical winding geometry, and finite conductor effects.

This work is limited to software-based validation against Ansys Maxwell. Physical experimental validation using real coil systems is identified as future work.

The remainder of the paper is organized as follows. Section 2 presents the theoretical formulation and extensions for non-coaxial coil systems. Section 3 describes the computational implementation and software-based validation methodology. Section 4 presents numerical and validation results. Section 5 discusses physical interpretation, limitations, and engineering implications. Section 6 concludes the paper.

2. THEORETICAL FRAMEWORK AND EXTENSION

This section presents the essential theoretical framework used for axial and radial magnetic-force prediction in practical air-core coil systems. To improve readability, only the equations required to define the magnetic-force formulation, coaxial reference model, misalignment transformation, force-component decomposition, practical winding representation, and surrogate-model mapping are retained in the main text. Detailed quadrature implementation, expanded rotation matrices, convergence definitions, and extended numerical-discretization details are provided in the computational-method section or may be supplied as supplementary material.

The formulation is based on magnetostatic field theory. The coils are assumed to be air-core systems with prescribed steady currents. Therefore, displacement current, radiation effects, eddy-current redistribution, skin effect, proximity effect, thermal deformation, and mechanical deformation are not included in the baseline model. These effects are identified as future extensions for high-frequency, thermally coupled, or mechanically coupled coil systems.

2.1. Magnetostatic Force Formulation

Consider two current-carrying air-core coils occupying volumes V_1 and V_2. Coil 1 carries current-density distribution $\mathbf{J}_1(\mathbf{r}_1)$ and produces a magnetic flux density $\mathbf{B}_1(\mathbf{r}_2)$ at a point $\mathbf{r}_2$ in Coil 2. Under magnetostatic conditions, the magnetic field generated by Coil 1 is obtained from the Biot-Savart law:

$$\mathbf{B}_1(\mathbf{r}_2) = \frac{\mu_0}{4\pi}\int_{V_1}\frac{\mathbf{J}_1(\mathbf{r}_1)\times(\mathbf{r}_2-\mathbf{r}_1)}{|\mathbf{r}_2-\mathbf{r}_1|^3}dV_1, \tag{1}$$

where $\mu_0 = 4\pi\times10^{-7}$ H/m is the permeability of free space, $\mathbf{r}_1$ a source point inside Coil 1, and $\mathbf{r}_2$ an observation point inside Coil 2.

The total magnetic force acting on Coil 2 is calculated from the Lorentz-force integral:

$$\mathbf{F}_{21} = \int_{V_2}\mathbf{J}_2(\mathbf{r}_2)\times\mathbf{B}_1(\mathbf{r}_2)dV_2, \tag{2}$$

where $\mathbf{J}_2(\mathbf{r}_2)$ is the current-density distribution in Coil 2. Substituting Eq. (1) into Eq. (2) gives the general coil-coil interaction force:

$$\begin{aligned}\mathbf{F}_{21} &= \frac{\mu_0}{4\pi}\int_{V_2}\int_{V_1}\mathbf{J}_2(\mathbf{r}_2)\times\frac{\mathbf{J}_1(\mathbf{r}_1)\times\mathbf{R}}{|\mathbf{R}|^3}dV_1dV_2,\\ \mathbf{R} &= \mathbf{r}_2-\mathbf{r}_1.\end{aligned} \tag{3}$$

Equation (3) is the general force expression underlying the direct numerical method and filament-based method. It is valid for finite coil dimensions, arbitrary relative positions, practical winding paths, and non-coaxial configurations, provided that the magnetostatic approximation remains valid [1–4].

2.2. Coaxial Reference Formulation

The ideal reference case consists of two perfectly coaxial circular coils whose symmetry axes coincide with the global z-axis. In this configuration, cylindrical symmetry causes the transverse force components to vanish:

$$F_x = F_y = 0, \quad \mathbf{F}_{21} = F_z\hat{\mathbf{z}}. \tag{4}$$

For two coaxial circular loops with radii a and b, separated by axial distance s, the elliptic modulus is

$$k^2 = \frac{4ab}{(a+b)^2+s^2}. \tag{5}$$

The mutual inductance between the two coaxial circular loops is evaluated using Maxwell's classical elliptic-integral expression:

$$M(a,b,s) = \mu_0\sqrt{ab}\left[\left(\frac{2}{k}-k\right)K(k) - \frac{2}{k}E(k)\right], \quad (6)$$

where $K(k)$ and $E(k)$ are the complete elliptic integrals of the first and second kind, respectively. Eq. (6) is used here as a known reference expression rather than re-derived; it follows the classical formulation of Maxwell and is also given in standard inductance References [1, 11, 13].

The axial force between the two loops is obtained from the derivative of magnetic co-energy with respect to axial separation:

$$F_z^{\text{loop}} = I_1 I_2 \frac{\partial M(a,b,s)}{\partial s}, \quad (7)$$

where I_1 and I_2 are the currents in the two loops. For finite-volume coils, the loop-loop interaction in Eq. (7) is integrated or numerically summed over the radial and axial winding regions. This forms the basis of the semi-analytical method used in the present work [7–13, 23, 24].

2.3. Non-Coaxial Geometry and Force Decomposition

Practical coil systems may experience lateral offset, angular tilt, eccentric winding, vibration, or assembly tolerance. To describe these effects, Coil 1 is fixed in the global coordinate system, while Coil 2 is translated and rotated relative to Coil 1. A point in Coil 2 is transformed from its local coordinate system to the global system as

$$\begin{aligned}\mathbf{r}_2 &= \mathbf{d} + \mathbf{Q}\mathbf{r}_{2,\text{loc}}, \quad \mathbf{d} = [d_x, d_y, g]^T, \\ \mathbf{Q} &= \mathbf{R}_y(\theta_y)\mathbf{R}_x(\theta_x), \end{aligned} \quad (8)$$

where d_x and d_y are lateral offsets; g is the axial center-to-center separation; and θ_x and θ_y are tilt angles about the x- and y-axes, respectively. The rotation matrix $\mathbf{Q}$ is applied consistently to both conductor position and current direction.

For a general non-coaxial configuration, the magnetic-force vector is

$$\mathbf{F}_{21} = F_x\hat{x} + F_y\hat{y} + F_z\hat{z}. \quad (9)$$

The axial force is F_z. When lateral displacement is present, the transverse force can be resolved into radial and tangential components. The radial force is

$$F_r = \frac{F_x d_x + F_y d_y}{\sqrt{d_x^2 + d_y^2}}, \quad d_\perp = \sqrt{d_x^2 + d_y^2} \neq 0, \quad (10)$$

and the tangential force is

$$F_t = \frac{-F_x d_y + F_y d_x}{\sqrt{d_x^2 + d_y^2}}. \quad (11)$$

For perfectly coaxial coils, $d_x = d_y = 0$ and $\theta_x = \theta_y = 0$, so symmetry requires $F_x = F_y = F_r = F_t = 0$. These equations define the axial, radial, and tangential force components used throughout the software-validation study [15, 20]. The coil geometry, coordinate system, and misalignment definitions used in this study are illustrated in Figure 1.

2.4. Practical Winding and Filament Representation

The ideal continuous-current model assumes that the coil current is purely azimuthal. A practical wound coil, however, consists of discrete turns following a helical conductor path. For a helical conductor of radius ρ, pitch p, and angular coordinate ϕ, the local current-direction unit vector can be written as

$$\hat{t} = \cos\alpha\hat{\phi} + \sin\alpha\hat{z}, \quad \tan\alpha = \frac{p}{2\pi\rho}, \quad (12)$$

where α is the winding pitch angle. For the baseline coil geometry used in this study, $p = 1.25\,\text{mm/turn}$ and $\rho = 54\,\text{mm}$, giving

$$\alpha = \tan^{-1}\left(\frac{0.00125}{2\pi(0.054)}\right) \approx 0.211^\circ. \quad (13)$$

Although this pitch angle is small, the helical representation improves agreement with finite-element software because it more accurately represents the actual conductor path, turn-to-turn spacing, and conductor placement.

For the filament-based method, each coil is represented by discrete current-carrying line segments. The total interaction force is approximated as

$$\mathbf{F}_{21} \approx \frac{\mu_0}{4\pi}\sum_{m=1}^{N_{s2}}\sum_{n=1}^{N_{s1}} I_m I_n \Delta\boldsymbol{\ell}_{2,m} \times \frac{\Delta\boldsymbol{\ell}_{1,n} \times \mathbf{R}_{mn}}{|\mathbf{R}_{mn}|^3}, \quad (14)$$

where N_{s1} and N_{s2} are the numbers of conductor segments in Coil 1 and Coil 2; I_m and I_n are segment currents; $\Delta\boldsymbol{\ell}_{1,n}$ and $\Delta\boldsymbol{\ell}_{2,m}$ are segment vectors; and $\mathbf{R}_{mn}$ is the separation vector between segment centers. Finite conductor diameter is included by subdividing each conductor into subfilaments while preserving the total current. This practical winding representation provides a bridge between ideal analytical models and detailed finite-element software simulations [16, 19, 24, 25].

2.5. Surrogate-Model Formulation

Detailed numerical integration, filament-based summation, and finite-element software simulation can become computationally expensive during repeated parameter sweeps and optimization. Therefore, a surrogate model is used to approximate the mapping from coil geometry and operating conditions to magnetic-force components:

$$[F_x, F_y, F_z]^T = \mathcal{M}_{\text{ML}}(\mathbf{x}), \quad (15)$$

where $\mathbf{x}$ contains the coil radii, coil lengths, turn numbers, currents, axial separation, lateral offsets, tilt angles, winding pitches, and conductor diameters. The radial and tangential forces are then calculated from F_x, F_y, d_x, and d_y using Eqs. (10) and (11).

In this work, the surrogate model is used only as a fast interpolation tool within the validated training domain. Extrapolation outside the sampled parameter space is not permitted because the surrogate does not explicitly solve the underlying electromagnetic field equations. This limitation is important for maintaining physical reliability during design-space exploration [17, 18, 21].

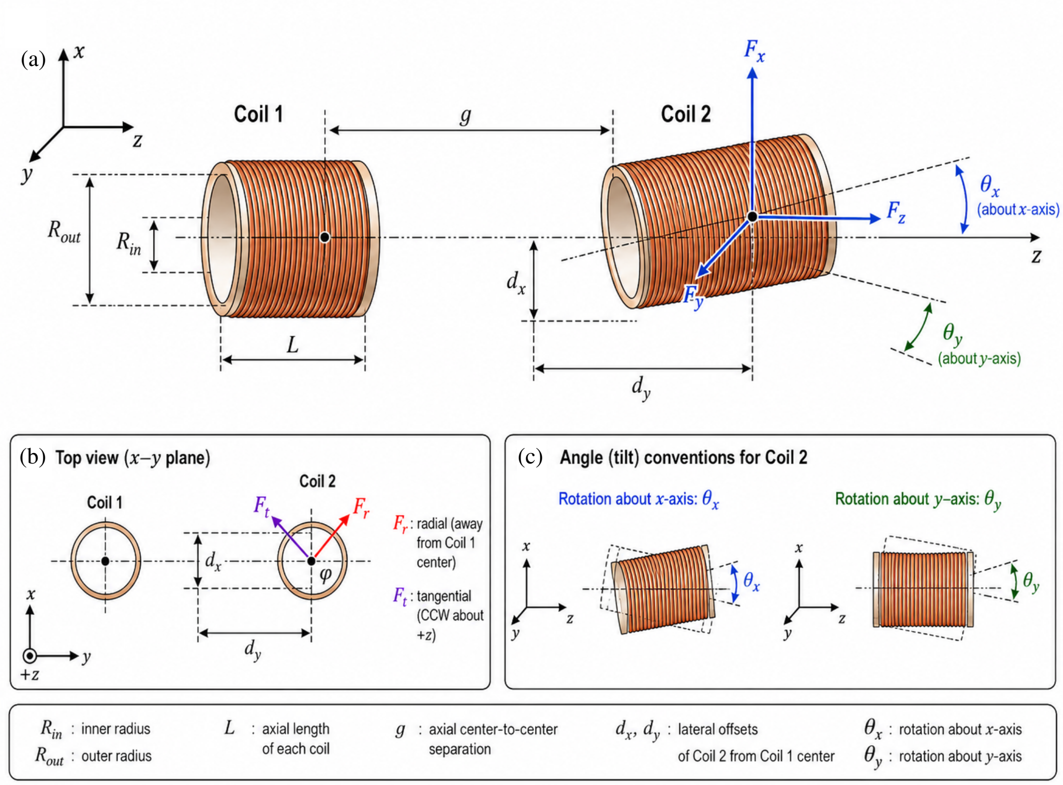

FIGURE 1. Coil geometry and coordinate system. The figure shows the air-core coil pair, axial separation g, lateral offsets d_x and d_y, tilt angles θ_x and θ_y, and force components F_x, F_y, F_z, F_r, and F_t. The angle convention is defined such that θ_x is rotation about the x-axis and θ_y is rotation about the y-axis.

2.6. Scope and Validity

The proposed framework is valid under the following assumptions. First, the excitation is magnetostatic or quasi-static, so displacement current, radiation, and transient wave effects are neglected. Second, the baseline analytical and filament-based models assume an air-core medium with relative permeability $\mu_r = 1$. Third, the current distribution is prescribed; skin effect, proximity effect, eddy-current redistribution, thermal variation, and current nonuniformity are not included. Fourth, overlapping conductor volumes are excluded to avoid near-singular current-element interactions. Fifth, the surrogate model is restricted to the validated training range.

Within these assumptions, the framework provides a compact theoretical basis for axial and radial force prediction in practical air-core coil systems. The following sections describe the computational implementation, Ansys Maxwell software-validation procedure, convergence assessment, and surrogate-model evaluation.

3. COMPUTATIONAL IMPLEMENTATION AND SOFTWARE-BASED VALIDATION

The proposed framework was computationally implemented to predict both axial and radial magnetic forces in practical air-core coil systems. It incorporates three independent physics-based approaches—a semi-analytical elliptic-integral formulation, direct numerical integration, and a filament-based discrete-winding model—together with a feedforward neural-network surrogate model developed for rapid force prediction.

The physics-based calculations and surrogate-model predictions were evaluated against finite-element electromagnetic simulations performed in Ansys Maxwell. These simulations served as an independent software-based reference for assessing the accuracy of the proposed methods over a wide range of coil configurations and operating conditions.

To ensure consistent and reproducible comparisons, all methods were evaluated using identical coil geometries, current excitations, axial separations, lateral offsets, angular tilts, and winding representations. Unless otherwise specified, all dimensional and physical quantities are expressed in the International System of Units (SI). Detailed mathematical derivations, grid-refinement results, extended convergence tables, and supplementary implementation settings are provided in the Supplementary Material to maintain the conciseness of the main manuscript.

3.1. Computational Workflow

The computational workflow begins by defining the coil geometry, current excitation, relative coil configuration, and winding representation. The force components are then calculated using the semi-analytical, direct numerical, and filament-based methods. The same geometry and excitation are implemented in Ansys Maxwell to provide an independent finite-element software reference. After software validation, the validated dataset is used to train and test the surrogate model.

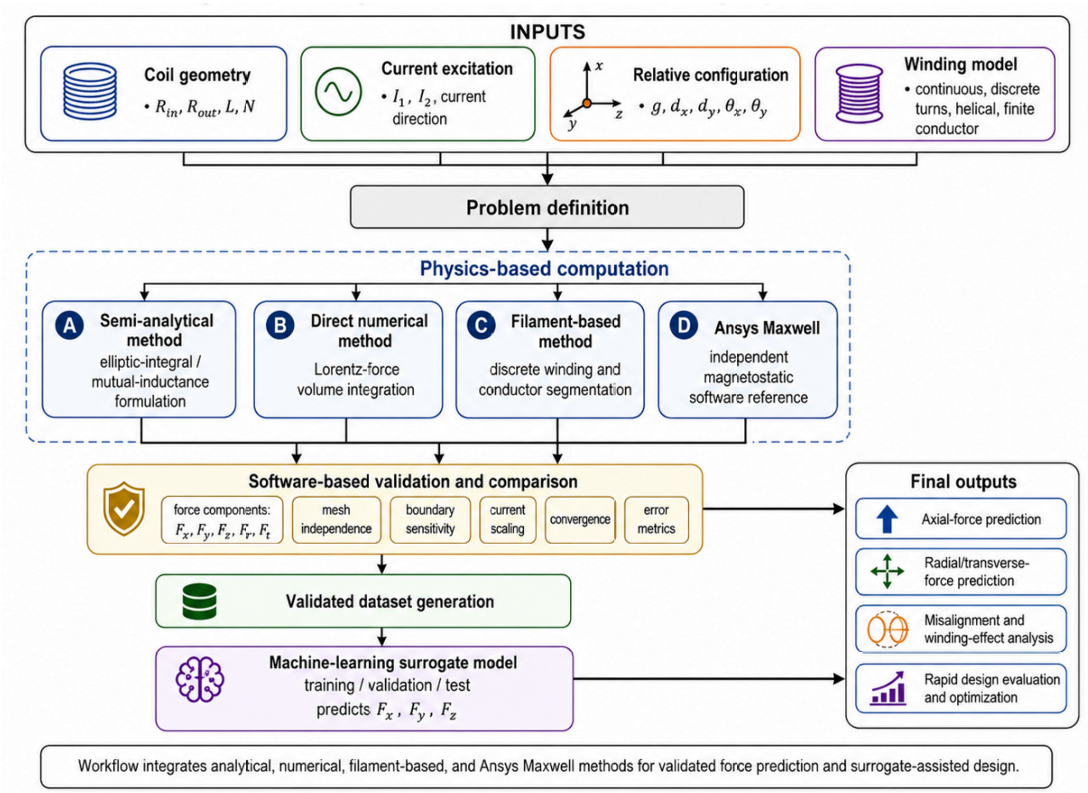

FIGURE 2. Computational workflow of the proposed framework. The workflow integrates coil geometry definition, current excitation, relative configuration, winding representation, semi-analytical computation, direct numerical integration, filament-based modeling, Ansys Maxwell software validation, validated dataset generation, surrogate-model training, and final force prediction.

The complete force vector is written as

$$\mathbf{F} = F_x\hat{x} + F_y\hat{y} + F_z\hat{\mathbf{z}}, \tag{16}$$

where F_z is the axial force, and F_x and F_y are transverse force components. When lateral offset is present, the radial and tangential force components are calculated using the force-decomposition equations defined in Section 2. The complete computational workflow of the proposed framework is shown in Figure 2.

3.2. Baseline Coil Geometry and Validation Domain

The validation geometry consists of two identical air-core coils. The baseline dimensions and operating conditions are summarized in Table 1. All dimensions are converted to SI units before computation.

The coils were selected to represent a moderate-size finite-volume air-core coil pair suitable for axial-force, radial-force, misalignment, winding-effect, and software-validation studies. The identical baseline geometry allows changes in force behavior to be attributed primarily to separation distance, lateral offset, angular tilt, current excitation, and winding representation.

3.3. Physics-Based Computational Method

Three physics-based methods are implemented.

The **semi-analytical method** uses the elliptic-integral mutual-inductance expression in Section 2. It is used mainly for coaxial and near-coaxial cases because it provides fast benchmark calculations. For finite-width coils, the radial and axial winding regions are discretized using 24×24 quadrature points.

The **direct numerical-integration method** evaluates the Lorentz-force interaction integral directly over the finite coil volume. The coil volume is discretized in the radial, angular, and axial directions using N_ρ, N_ϕ, and N_z points. The finest direct numerical grid used for the representative validation case is $N_\rho = 24$, $N_\phi = 144$, and $N_z = 24$.

The filament-based method represents each coil as a set of current-carrying conductor segments. This method is used to model discrete turns, helical pitch, finite conductor diameter, conductor spacing, and non-coaxial alignment. For the fine filament model, each turn is divided into 240 segments, and each conductor is represented by 4 subfilaments. Therefore, the total number of segment elements per coil is

$$N_{\text{seg,total}} = 200 \times 240 \times 4 = 192000. \tag{17}$$

The filament method provides a practical bridge between ideal analytical models and finite-element software models with explicit conductor geometry.

3.4. Practical Usage Guide for the Computational Method

To clarify the role of each method, Table 2 summarizes when each modeling level should be used. This table is included to make the framework easier to apply and to address the need for a concise practical summary.

TABLE 1. Coil dimensions and operating conditions used in the validation study.

Parameter	Symbol	Coil 1	Coil 2
Inner radius	R_{in}	50 mm	50 mm
Outer radius	R_{out}	58 mm	58 mm
Mean radius	R_{mean}	54 mm	54 mm
Radial winding thickness	t_r	8 mm	8 mm
Axial length	L	50 mm	50 mm
Number of turns	N	200	200
Approximate turns per layer	N_{layer}	40	40
Approximate radial layers	N_{radial}	5	5
Nominal current	I	6 A	6 A
Nominal ampere-turns	NI	1200 A-turns	1200 A-turns
Bare conductor diameter	d_c	1.20 mm	1.20 mm
Effective insulated wire diameter	d_{ins}	1.25 mm	1.25 mm
Winding pitch	p	1.25 mm/turn	1.25 mm/turn
Turn-to-turn insulation spacing	s	0.05 mm	0.05 mm
Core material	-	Air core	Air core
Relative permeability	μ_r	1	1
Current direction for attractive case	-	Counterclockwise viewed from $+z$	Counterclockwise viewed from $+z$
Axial separation range	g	60–180 mm	60–180 mm
Representative axial separation	g_0	100 mm	100 mm
Lateral offset range	d_x	-20 to $+20$ mm	-20 to $+20$ mm
Secondary lateral offset	d_y	0 mm for main sweep; optional ± 10 mm	0 mm for main sweep; optional ± 10 mm
Angular tilt range	θ_x, θ_y	0°–10°	0°–10°
Current-scaling sweep	I_1, I_2	2, 4, 6, 8 A	2, 4, 6, 8 A
Minimum non-overlap condition	-	$g_{\text{min}} = 60\,\text{mm} > L = 50\,\text{mm}$	$g_{\text{min}} = 60\,\text{mm} > L = 50\,\text{mm}$

TABLE 2. Practical usage guide for the proposed method.

Method	Recommended use	Main advantage	Main limitation
Semi-analytical elliptic-integral method	Coaxial and near-coaxial preliminary design	Very fast and transparent	Limited for strong misalignment and detailed winding geometry
Direct numerical integration	Physics-based verification and benchmark cases	Direct Lorentz-force evaluation	Higher computational cost
Filament-based method	Practical winding, helical pitch, and finite conductor effects	Captures real winding features	Requires segment and subfilament convergence
Ansys Maxwell simulation	Independent finite-element software validation	High-fidelity numerical benchmark	Requires mesh and boundary convergence
Surrogate model	Repeated prediction and optimization inside training domain	Extremely fast after training	Interpolation only; no extrapolation

3.5. Ansys Maxwell Software-Validation Setup

Independent finite-element software simulation is performed in Ansys Maxwell using the same coil dimensions, current excitation, winding representation, axial separation, lateral offset, and angular tilt used in the physics-based models. The simulations are magnetostatic, and the surrounding medium is air with $\mu_r = 1$. The software force is extracted using Lorentz-force integration, with Maxwell stress tensor evaluation available as a consistency check.

The Ansys Maxwell model, mesh refinement strategy, and air-domain boundary definition are shown in Figure 3.

The main Ansys Maxwell settings and software-validation criteria are summarized in Table 3.

The extra-fine mesh and the largest air domain are used as the software-validation reference after mesh-independence and boundary-domain sensitivity checks.

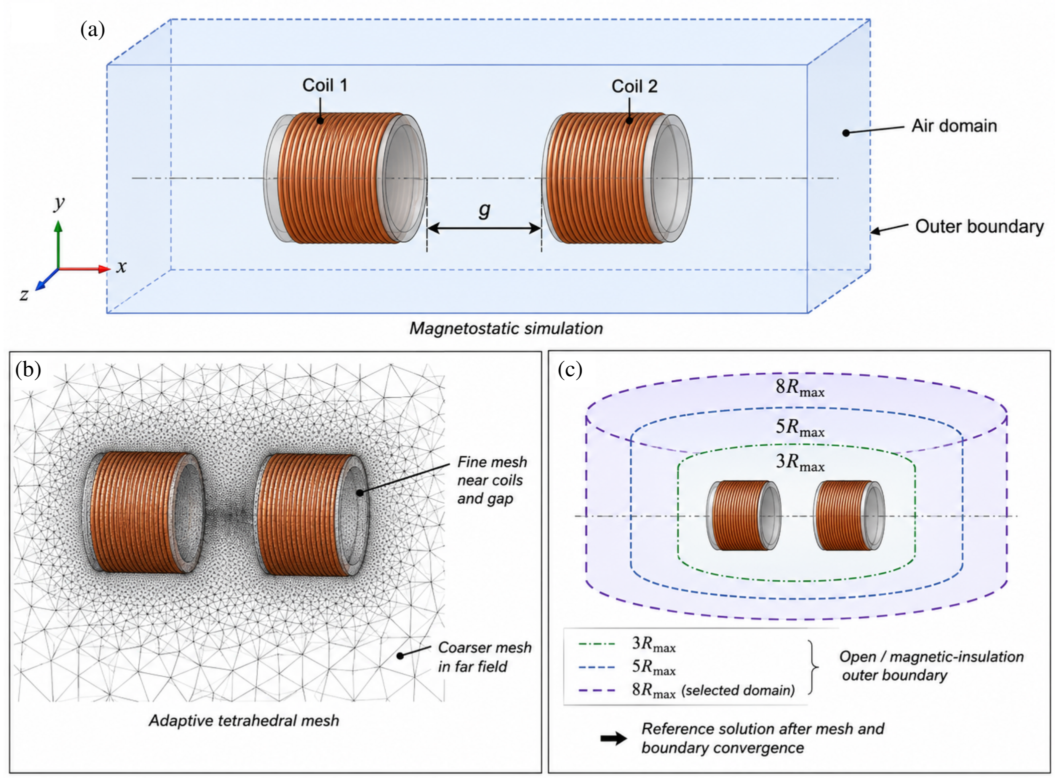

FIGURE 3. Ansys Maxwell model, mesh, and air-domain boundary. The figure shows the representative finite-element software setup, including the air-core coil geometry, adaptive tetrahedral mesh refinement near the coils and gap region, and the surrounding air-domain boundary used for boundary-sensitivity evaluation.

3.6. Validation Metrics

The model-to-software vector error is calculated as

$$\varepsilon_F = \frac{\|\mathbf{F}_{\text{model}} - \mathbf{F}_{\text{Maxwell}}\|}{\|\mathbf{F}_{\text{Maxwell}}\|} \times 100\%. \tag{18}$$

Here, $\mathbf{F}_{\text{model}}$ is the force vector predicted by the semi-analytical, direct numerical, filament-based, or surrogate model, and $\mathbf{F}_{\text{Maxwell}}$ is the corresponding Ansys Maxwell reference force vector.

Agreement among the three physics-based methods is evaluated using the relative half-spread:

$$\delta_{\text{HS}} = \frac{F_{\text{max}} - F_{\text{min}}}{2F_{\text{mean}}} \times 100\%, \tag{19}$$

where F_{max}, F_{min}, and F_{mean} are calculated from the semi-analytical, direct numerical, and filament-based force predictions.

The current-scaling behavior is checked using the magnetostatic proportionality

$$F \propto I_1 I_2. \tag{20}$$

For example, doubling both currents should increase force magnitude by approximately a factor of four. Reversing one current direction should reverse the force sign. These checks verify the excitation definition and force-sign convention.

The offset sign-symmetry error is evaluated using equal positive and negative lateral offsets:

$$\varepsilon_{\text{sym}} = \frac{|F_r(+d_x) + F_r(-d_x)|}{0.5\left(|F_r(+d_x)| + |F_r(-d_x)|\right)} \times 100\%. \tag{21}$$

A small value of ε_{sym} confirms that the radial-force direction changes consistently when the offset direction is reversed.

3.7. Surrogate-Model Implementation

A feedforward neural network is used as a surrogate model to accelerate repeated force prediction. The input variables include coil radii, coil lengths, number of turns, currents, axial separation, lateral offsets, tilt angles, winding pitch, and conductor diameter. The output variables are F_x, F_y, and F_z. The radial and tangential force components are then calculated from F_x, F_y, d_x, and d_y.

A feedforward neural network was selected because the mapping among geometry, current excitation, misalignment, winding parameters, and force components is nonlinear but smooth within the sampled design domain. Gaussian-process regression was not selected because its computational cost increases rapidly with dataset size, especially for 12000 samples. Physics-informed neural networks were not used because the surrogate is not intended to solve the electromagnetic field equations directly; instead, it is used as a fast interpolation model trained on validated force data. Therefore, a compact

TABLE 3. Ansys Maxwell simulation setup and software-reference criteria.

Item	Setting used in this study
Software	Ansys Maxwell within Ansys Electronics Desktop 2026 R1 [22]
Solver type	Magnetostatic
Medium	Air, $\mu_r = 1$
Conductor material	Copper or equivalent current-carrying coil region
Excitation	Prescribed DC current
Force extraction	Lorentz-force integratio; Maxwell stress tensor used as consistency check when available
Mesh type	Adaptive tetrahedral mesh
Representative mesh levels	Coarse, medium, fine, extra-fine
Extra-fine mesh size	1.46×10^6 elements
Air-domain radii tested	$3R_{\max} = 174\,\text{mm}$, $5R_{\max} = 290\,\text{mm}$, $8R_{\max} = 464\,\text{mm}$
Boundary condition	Open boundary or magnetic-insulation outer boundary
Mesh-independence target	Final force-vector change below 2%
Boundary-sensitivity target	Final force-vector change below 1%
Achieved mesh-independence change	0.15%
Achieved boundary-domain sensitivity	0.12%

TABLE 4. Surrogate-model dataset and training configuration.

Item	Setting
Total valid samples	12000
Training data	70%, 8400 samples
Validation data	15%, 1800 samples
Test data	15%, 1800 samples
Network type	Feedforward neural network
Hidden layers	Two hidden layers
Neurons per hidden layer	50
Optimizer	Adam
Loss function	Mean-squared error
Input/output preprocessing	Normalization before training
Main outputs	F_x, F_y, F_z
Derived outputs	F_r, F_t, force-vector magnitude
Test-set performance target	Mean relative error below 5%, maximum error below 10%, $R^2 > 0.95$
Final achieved performance	$R^2 = 0.996$–0.998, mean error below 1.20% , maximum error 5.00%
Use limitation	Interpolation only within the sampled domain

feedforward neural network provides a suitable balance between accuracy, speed, and implementation simplicity.

The surrogate-model setup is summarized in Table 4.

The surrogate input domain is summarized in Table 5.

Extrapolation outside the sampled parameter space is not permitted, because the surrogate does not explicitly solve the underlying electromagnetic field equations and is valid only within the validated training domain.

3.8. Reproducibility and Supplementary Material

For reproducibility, the following information is reported in the main paper or supplementary material: coil dimensions,

TABLE 5. Surrogate-model input parameter range.

Parameter group	Variables	Range
Coil inner radius	$R_{1,\text{in}}, R_{2,\text{in}}$	45–60 mm
Radial winding thickness	t_{r1}, t_{r2}	6–12 mm
Coil axial length	L_1, L_2	40–70 mm
Number of turns	N_1, N_2	120–260
Coil current	I_1, I_2	2–8 A
Axial separation	g	60–180 mm
Lateral offset	d_x, d_y	$d_x = -20$ to $+20$ mm; $d_y = -10$ to $+10$ mm
Tilt angles	θ_x, θ_y	-10° to $+10^\circ$
Winding pitch	p_1, p_2	1.0–2.0 mm/turn
Wire diameter	$d_{c,1}, d_{c,2}$	0.8–1.6 mm
Relative permeability	μ_r	1

current magnitudes and directions, axial separation, lateral offsets, tilt angles, winding pitch, conductor diameter, numerical grid settings, filament segment density, Ansys Maxwell mesh statistics, air-domain size, boundary condition, force-extraction method, surrogate input ranges, dataset split, and final test-set metrics.

To keep the main manuscript focused, the following details should be provided as supplementary material:

- full direct numerical grid-refinement table,
- full filament convergence table,
- full Ansys Maxwell mesh-independence table,
- full boundary-domain sensitivity table,
- raw axial-force, radial-force, tilt-force, and current-scaling datasets,
- surrogate training ranges and normalization details,
- input files or scripts used to reproduce the validation cases, where possible.

This supplementary structure preserves research depth while reducing the main manuscript length and improving readability.

3.9. Summary

This section defines the computational and software-validation methodology used in the study. The semi-analytical method provides rapid benchmark predictions, the direct numerical method provides a physics-based Lorentz-force reference, and the filament-based method represents practical winding geometry. Ansys Maxwell is used as an independent finite-element software-validation reference after mesh-independence and boundary-domain sensitivity checks. A feedforward neural-network surrogate model is trained using validated simulation data for rapid interpolation within the sampled design domain.

The revised methodology is intentionally concise. It keeps the equations and parameters necessary for reproducibility while moving extended derivations, raw convergence data, and detailed numerical tables to supplementary material. This structure directly addresses the reviewer's concerns about excessive volume while preserving the technical quality of the research.

4. SOFTWARE-BASED VALIDATION RESULTS

This section presents the software-based validation results for the proposed computational framework. The validation is performed against independent finite-element simulations in Ansys Maxwell under identical geometric and electrical conditions. The purpose of this section is to demonstrate that the semi-analytical, direct numerical, filament-based, and surrogate-model predictions are consistent with the finite-element software reference.

The validation is limited to software-based validation. Physical experimental validation using real coil pairs is not claimed in this study and is identified as future work.

The baseline validation geometry consists of two identical air-core coils with inner radius $R_{\text{in}} = 50$ mm, outer radius $R_{\text{out}} = 58$ mm, mean radius $R_{\text{mean}} = 54$ mm, axial length $L = 50$ mm, number of turns $N = 200$, nominal current $I = 6$ A, winding pitch $p = 1.25$ mm/turn, and conductor diameter $d_c = 1.20$ mm. Unless otherwise stated, the representative validation condition is

$$g = 100\,\text{mm}, \quad d_x = 10\,\text{mm}, \quad d_y = 0, \quad \theta_x = \theta_y = 0^\circ. \tag{22}$$

The positive z-axis is defined from Coil 1 toward Coil 2. Therefore, for currents flowing in the same azimuthal direction, the force on Coil 2 is attractive and appears as a negative F_z value under the selected sign convention. When only magnitudes are compared, $|F_z|$, $|F_r|$, and $|\mathbf{F}|$ are reported.

Detailed numerical datasets for the axial-force sweep, radial-offset sweep, tilt sweep, current-scaling test, direct numerical convergence, filament convergence, and combined offset-and-tilt cases are provided in the Supplementary Material.

4.1. Stability of the Ansys Maxwell Reference Solution

Before using Ansys Maxwell as the software-validation reference, mesh-independence and boundary-domain sensitivity tests were performed. The representative case $g = 100$ mm, $d_x = 10$ mm, $d_y = 0$, and $\theta_x = \theta_y = 0^\circ$ was used because it includes both axial and radial force components.

The transverse-force ratio for the coaxial symmetry check is calculated as

$$\eta_\perp = \frac{\sqrt{F_x^2 + F_y^2}}{|\, F_z \,|} \times 100\%. \tag{23}$$

where F_x, F_y, and F_z are the transverse and axial force components obtained from the Ansys Maxwell solution. For a perfectly aligned coaxial configuration, cylindrical symmetry requires the transverse force components to approach zero.

The stability checks performed for the Ansys Maxwell reference solution are summarized in Table 6.

The final mesh-independence change of 0.15% and boundary-domain sensitivity of 0.12% confirm that the finite-element reference solution is stable. The coaxial transverse-force ratio remains below 0.010%, confirming that

TABLE 6. Stability checks for the Ansys Maxwell software reference.

Validation check	Test condition	Achieved value	Acceptance criterion	Status
Mesh-independence test	Coarse to extra-fine mesh, up to 1.46×10^6 elements	0.15% final vector change	$< 2\%$	Passed
Boundary-domain sensitivity	$3R_{\text{max}}$, $5R_{\text{max}}$, and $8R_{\text{max}}$, with $R_{\text{max}} = 58\,\text{mm}$	0.12% final vector change	$< 1\%$	Passed
Coaxial transverse-force ratio	$g = 60$–$180\,\text{mm}$, $d_x = d_y = 0$	0.010% maximum	$< 1\%$ of $\mid F_z \mid$	Passed
Current-scaling check	$I_1, I_2 = 2, 4, 6, 8\,\text{A}$	0.77% maximum error	$< 5\%$	Passed

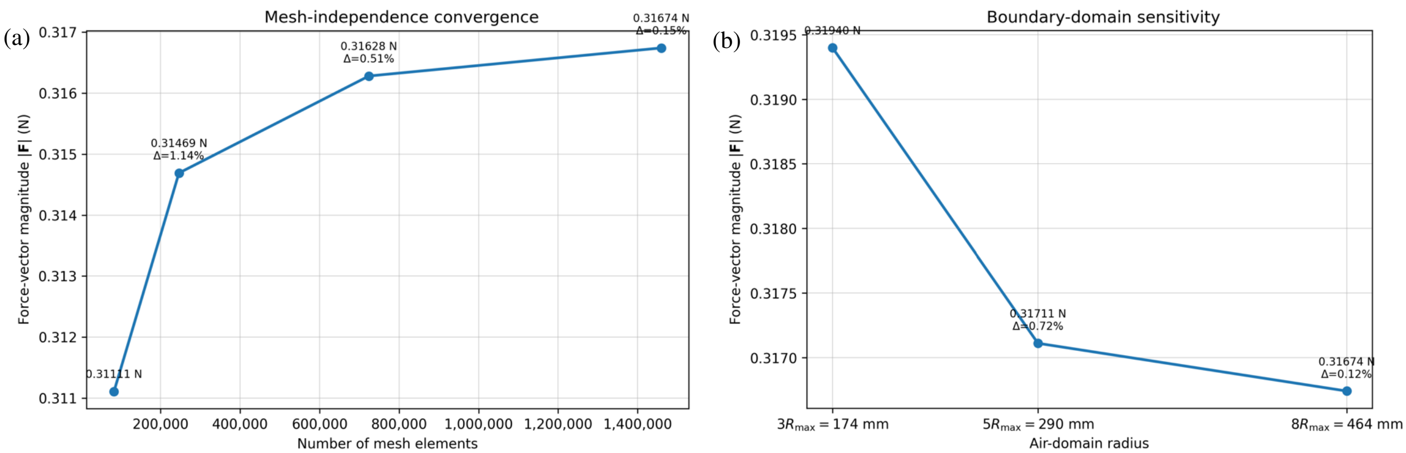

FIGURE 4. Mesh-independence and boundary-domain convergence. The force-vector magnitude converges with mesh refinement and air-domain expansion. The final mesh-independence change is 0.15%, and the final boundary-domain sensitivity is 0.12%, confirming that the Ansys Maxwell reference solution is stable for software validation.

the software model preserves cylindrical symmetry under perfect alignment.

The mesh-independence and boundary-domain convergence behavior are presented in Figure 4.

4.2. Axial-Force and Radial-Force Validation

For the coaxial validation case, the coils are perfectly aligned:

$$d_x = d_y = 0, \;\; \theta_x = \theta_y = 0^\circ. \tag{24}$$

In this configuration, cylindrical symmetry requires $F_x = F_y = 0$, and only the axial force F_z remains. The axial force was evaluated for $g = 60$–$180\,\text{mm}$. The results show that $|F_z|$ decreases monotonically as the axial separation increases. This is physically expected because magnetic coupling decreases as the coil separation increases. The maximum relative deviation among the semi-analytical, direct numerical, filament-based, Ansys Maxwell, and surrogate predictions is 0.62%. The axial-force variation with axial separation is shown in Figure 5.

For the lateral-offset validation case, the axial separation is fixed at $g = 100\,\text{mm}$, and the lateral offset is varied over $d_x = -20 + 20\,\text{mm}$. For $d_y = 0$, the radial force is equivalent to the x-component of the force:

$$F_r = F_x. \tag{25}$$

The radial force is zero at perfect alignment and increases in magnitude as $|d_x|$ increases. Reversing the offset direction reverses the sign of the radial force. The maximum radial-force sign-symmetry error is 0.23%, which confirms correct implementation of the radial-force direction. The radial-force response under lateral offset is shown in Figure 6.

4.3. Angular and Combined Misalignment Validation

Angular misalignment was evaluated by varying θ_x from 0° to 10°, while keeping $d_x = d_y = 0$ and $\theta_y = 0^\circ$. The axial force magnitude decreases slightly as the tilt angle increases, while the transverse force magnitude increases. In the Ansys Maxwell reference data, $|F_z|$ decreases from $0.31920\,\text{N}$ at 0° to $0.30567\,\text{N}$ at 10°, while $F_\perp$ increases from 0 to $0.04115\,\text{N}$. This confirms that angular misalignment breaks the coaxial symmetry and generates transverse force components. The influence of angular misalignment on force components is shown in Figure 7.

Combined offset-and-tilt validation was performed by applying lateral offset and angular tilt simultaneously. Across combined misalignment cases, the maximum vector-force error relative to Ansys Maxwell is 0.42%. This value is well below the selected 8% acceptance criterion for angular-misalignment

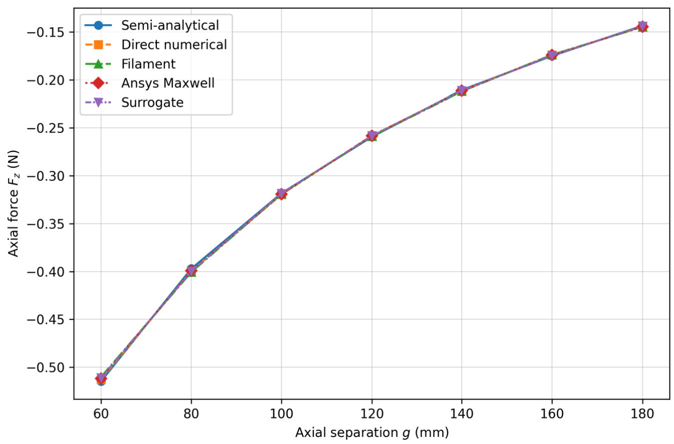

FIGURE 5. Axial force versus axial separation. The axial force decreases in magnitude as the coil separation g increases. The close overlap among the semi-analytical, direct numerical, filament-based, Ansys Maxwell, and surrogate results confirms strong agreement for the coaxial validation case.

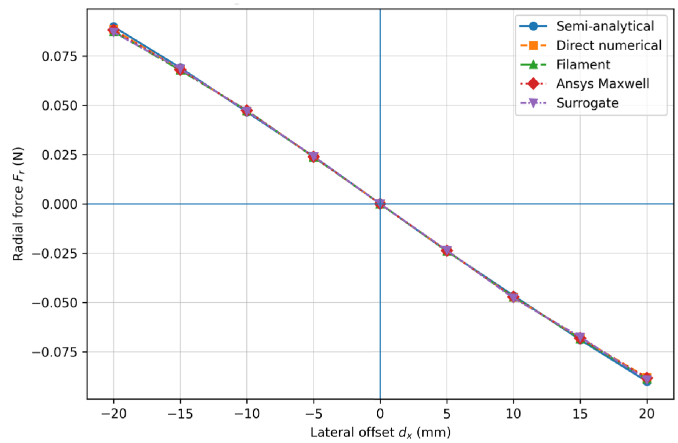

FIGURE 6. Radial force versus lateral offset. The radial force is zero at perfect alignment and reverses sign when the lateral-offset direction is reversed. This confirms the expected radial-force symmetry under positive and negative offset.

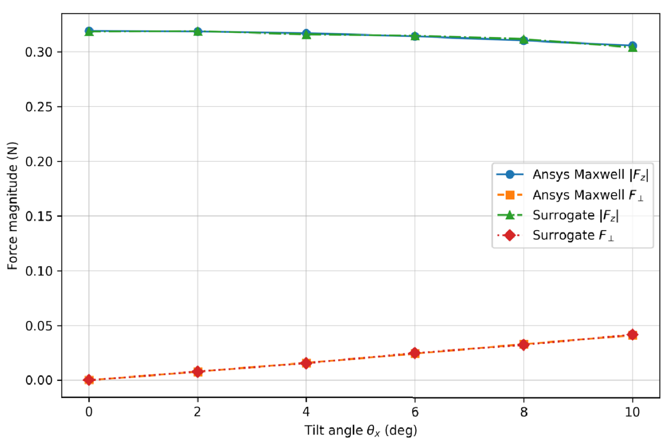

FIGURE 7. Effect of angular misalignment on force components. The axial force magnitude decreases slightly as the tilt angle increases, while the transverse-force component increases with angular misalignment.

cases and confirms that the framework can evaluate general non-coaxial force behavior.

4.4. Practical Winding-Model Comparison

The influence of winding representation was evaluated for the representative misaligned case $g = 100\,\text{mm}$ and $d_x = 10\,\text{mm}$. Five winding representations were compared: continuous current region, discrete circular turns, helical winding pitch, finite conductor diameter, and full practical winding.

The influence of different winding representations on the agreement with Ansys Maxwell is summarized in Table 7.

The vector error decreases from 2.87% for the continuous-current approximation to 0.10% for the full practical winding model. This result shows that practical winding representation can dominate the remaining model-to-software discrepancy after mesh and boundary convergence have been achieved.

Although the baseline helical pitch angle is small, approximately $0.211°$, the helical model improves agreement because it better represents the actual conductor path, turn placement, and finite winding geometry used in the finite-element model. The influence of practical winding representation on model accuracy is shown in Figure 8.

4.5. Agreement Among Physics-Based Methods

The semi-analytical, direct numerical, and filament-based methods were compared under identical geometric and electrical conditions. The maximum relative half-spread among the three physics-based methods is 0.55%, which is well below the selected 5% acceptance criterion. This confirms strong internal consistency among the independent physics-based implementations.

The direct numerical method and filament-based method also show stable convergence. The final direct numerical refinement changes the force magnitude by 0.09%, and the final filament-method refinement also changes the force magnitude by 0.09%. These results confirm that the selected numerical grid and filament discretization are sufficient for the validation cases.

The average model-to-software relative errors are 1.35% for the semi-analytical method, 0.46% for the direct numerical method, 0.72% for the filament-based method, and 1.08% for the surrogate model. The maximum model-to-software error among all reported methods is 4.86%, which is below the selected 10% acceptance criterion.

4.6. Surrogate-Model Prediction Accuracy

The surrogate model was trained using 12000 validated samples, divided into 70% training data, 15% validation data, and 15% test data. The test dataset was not used during training. The surrogate predicts F_x, F_y, and F_z, while F_r, F_t, and $|\mathbf{F}|$ are derived from the predicted force components. The surrogate-

TABLE 7. Influence of winding representation on agreement with Ansys Maxwell.

Winding representation	Main included effect	Vector error relative to Ansys Maxwell (%)
Continuous current region	Homogenized azimuthal current density	2.87
Discrete circular turns	Turn discretization	1.54
Helical winding pitch	Axial component of helical conductor path	0.71
Finite conductor diameter	Finite wire cross-section	0.27
Full practical winding	Discrete turns, pitch, conductor diameter, and placement	0.10

TABLE 8. Surrogate-model prediction accuracy on the test dataset.

Output	RMSE (N)	Mean relative error (%)	Maximum relative error (%)	R^2
F_x	0.0021	1.03	4.82	0.997
F_y	0.0020	1.10	4.91	0.996
F_z	0.0040	0.95	4.50	0.998
F_r	0.0023	1.20	5.00	0.996
$\|\mathbf{F}\|$	0.0045	0.88	4.36	0.998

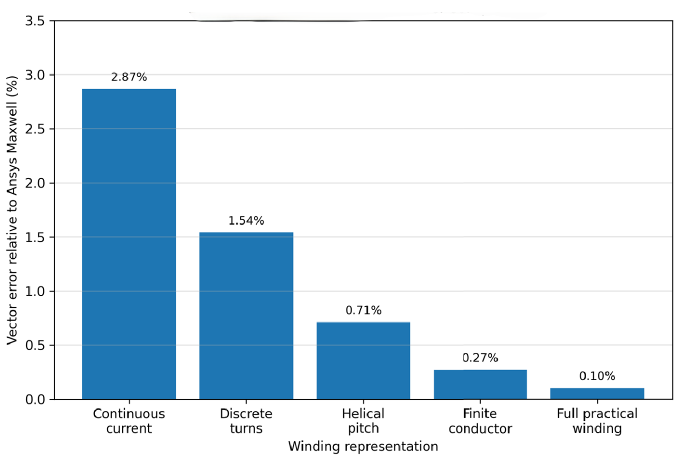

FIGURE 8. Practical winding model comparison. The model-to-software vector error decreases from 2.87% for the continuous-current approximation to 0.10% for the full practical winding model, demonstrating the benefit of including discrete turns, helical pitch, and finite conductor effects.

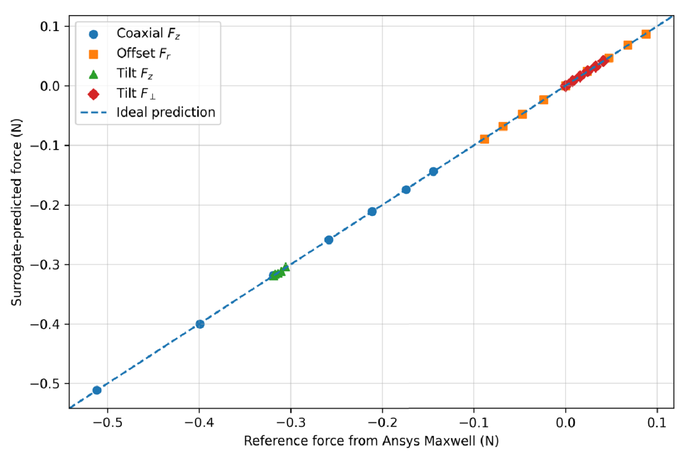

FIGURE 9. Surrogate-model prediction accuracy. The surrogate-model predictions are compared with representative Ansys Maxwell reference force values. The close clustering of points near the ideal prediction line confirms accurate interpolation within the validated design domain.

model prediction accuracy on the independent test dataset is summarized in Table 8.

The surrogate model achieves $R^2 = 0.996$–0.998, mean relative error below 1.20%, and maximum relative error of 5.00% on unseen test data. These results confirm that the surrogate model is accurate within the validated training domain. The surrogate-model prediction accuracy compared with Ansys Maxwell reference results is shown in Figure 9.

The surrogate model is used only for interpolation within the sampled parameter range. It is not used for extrapolation outside the validated training domain.

4.7. Summary of Validation Outcomes

The principal validation outcomes are summarized in Table 9. All achieved values satisfy the acceptance criteria defined in Section 3.

The results demonstrate that the proposed framework provides stable and accurate software-validated force predictions for the investigated air-core coil configurations. The framework captures coaxial axial-force behavior, radial-force generation under lateral offset, transverse-force growth under angular misalignment, combined offset-and-tilt behavior, practical

TABLE 9. Summary of software-based validation outcomes.

Validation item	Achieved result	Acceptance criterion	Status
Software mesh-independence change	0.15%	$< 2\%$	Passed
Boundary-domain sensitivity	0.12%	$< 1\%$	Passed
Direct numerical final refinement change	0.09%	< 2–3%	Passed
Filament final refinement change	0.09%	$< 3\%$	Passed
Maximum relative half-spread among physics-based methods	0.55%	$< 5\%$	Passed
Maximum axial-force deviation in coaxial sweep	0.62%	$< 5\%$	Passed
Maximum radial-force sign-symmetry error	0.23%	$< 5\%$	Passed
Maximum combined offset-and-tilt vector error	0.42%	$< 8\%$	Passed
Maximum current-scaling error	0.77%	$< 5\%$	Passed
Practical winding error reduction	2.87% to 0.10%	Error decreases	Passed
Average model-to-software error	0.46–1.35%	$< 5\%$	Passed
Maximum model-to-software error	4.86%	$< 10\%$	Passed
Surrogate mean relative error	0.88–1.20%	$< 5\%$	Passed
Surrogate maximum relative error	5.00%	$< 10\%$	Passed
Surrogate coefficient of determination	$R^2 = 0.996$–0.998	$> 0.95\%$	Passed

winding effects, current scaling, and surrogate-model prediction accuracy.

Overall, the validation confirms that the proposed software-validated framework is reliable for axial and radial magnetic-force prediction in practical air-core coil systems within the investigated parameter range.

5. DISCUSSION

This section discusses the significance of the software-based validation results and clarifies the practical meaning, limitations, and intended use of the proposed framework. The main objective of the work is to extend ideal coaxial coil-force analysis toward practical air-core coil systems with lateral offset, angular tilt, radial force components, discrete winding geometry, finite conductor effects, and surrogate-assisted rapid prediction.

The present work is explicitly a software-based validation study. The proposed semi-analytical, direct numerical, filament-based, and surrogate-model predictions are validated against independent finite-element simulations in Ansys Maxwell. Physical experimental validation using real-coil pairs is not claimed in this paper and is identified as future work.

5.1. Physical Interpretation of the Validation Results

The validation results confirm that the proposed framework captures the expected physical behavior of interacting air-core coils. For perfectly coaxial coils, cylindrical symmetry causes the transverse force components to vanish, and the magnetic interaction is dominated by the axial force. The axial-force magnitude decreases monotonically as the axial separation increases, which is consistent with classical mutual-inductance and elliptic-integral coil-force theory [1–3, 7–13, 23, 24]. In the coaxial separation sweep, the maximum relative deviation among the semi-analytical, direct numerical, filament-based, Ansys Maxwell, and surrogate predictions is 0.62%, confirming strong agreement for the axial-force benchmark.

When lateral offset is introduced, the cylindrical symmetry is broken, and a radial force component appears. The radial force is zero at perfect alignment, increases in magnitude with lateral displacement, and changes sign when the offset direction is reversed. The maximum radial-force sign-symmetry error is 0.23%, which is well below the selected 5% acceptance criterion. This confirms that the coordinate transformation and radial-force decomposition are physically consistent.

Angular misalignment also produces transverse force components. As the tilt angle increases, the axial-force magnitude decreases slightly, while the transverse-force magnitude increases. This behavior is expected because angular tilt changes both the relative positions of current elements and their current-direction vectors. Combined offset-and-tilt cases show vector-force errors below 0.50%, with a maximum reported value of 0.42%. This indicates that the framework can handle general non-coaxial coil configurations rather than only ideal coaxial arrangements.

5.2. Agreement among Computational Methods

The three physics-based methods provide complementary levels of modeling detail. The semi-analytical elliptic-integral method is the fastest and most transparent for coaxial and near-coaxial configurations. The direct numerical method evaluates the Lorentz-force interaction more generally and provides a useful physics-based reference. The filament-based method is more suitable for practical wound coils because it can represent discrete turns, helical pitch, finite conductor diameter, conductor spacing, and local conductor placement.

The maximum relative half-spread among the three physics-based methods is 0.55%, which is far below the selected 5% acceptance criterion. This small spread indicates that the independent computational implementations are mutually consistent. The direct numerical and filament-based methods also show stable convergence, with final refinement changes of 0.09% in both cases.

The Ansys Maxwell simulations provide an independent finite-element software reference. The final mesh-independence change is 0.15%, and the final boundary-domain sensitivity is 0.12%. These values confirm that the software reference solution is stable before it is used for validation. The average model-to-software errors are 1.35% for the semi-analytical method, 0.46% for the direct numerical method, 0.72% for the filament-based method, and 1.08% for the surrogate model. The maximum model-to-software error is 4.86%, which is below the selected 10% limit.

These results show that the proposed framework is not dependent on a single modeling approach. Instead, its strength comes from agreement among multiple computational levels and an independent finite-element software reference.

5.3. Importance of Practical Winding Representation

The practical winding comparison demonstrates that winding representation has a measurable effect on force prediction. The continuous-current model assumes a homogenized azimuthal current distribution. This approximation is useful for rapid calculations, but it does not explicitly represent discrete turns, helical pitch, finite wire diameter, insulation spacing, or conductor placement.

Including practical winding details reduces the model-to-software vector error from 2.87% for the continuous-current approximation to 0.10% for the full practical winding model. This improvement is important because it shows that winding representation can dominate the remaining discrepancy after mesh and boundary convergence have already been achieved.

The helical pitch angle in the baseline coil is small, approximately 0.211°, because the winding pitch is 1.25 mm/turn, and the mean coil radius is 54 mm. Although this angle is small, the helical representation still improves agreement because it better matches the actual conductor trajectory used in the finite-element model. The improvement is not caused only by the axial component of current; it also reflects more accurate turn placement, conductor spacing, and finite winding geometry.

This result supports the use of the filament-based method as a bridge between ideal analytical models and high-fidelity finite-element simulations. It provides a practical way to include winding-level geometry while remaining much faster than repeated full-field software simulation.

5.4. Surrogate Model and Design Use

The feedforward neural-network surrogate model was introduced to accelerate repeated force prediction and design-space exploration. The surrogate is trained using 12000 validated samples and predicts F_x, F_y, and F_z. The derived quantities, including radial force and total force magnitude, are then computed from these predicted components.

The surrogate achieves $R^2 = 0.996$–0.998, mean relative error below 1.20%, and maximum relative error of 5.00% on unseen test data. These values indicate that the surrogate accurately interpolates within the validated design domain. The surrogate also satisfies important physical symmetry checks: transverse forces remain close to zero under coaxial alignment, and the radial force changes sign when the lateral offset is reversed.

The surrogate model is useful for rapid design studies, optimization, and sensitivity analysis because it avoids repeated finite-element simulations after training. The average Ansys Maxwell simulation time is approximately 215 s per case, while the surrogate prediction time is approximately 8.5×10^{-4} s, corresponding to a speed-up of about 2.53×10^5.

However, the surrogate should be treated strictly as an interpolation tool. It should not be used outside the sampled parameter range because it does not explicitly solve the electromagnetic field equations. Extrapolation beyond the validated training domain may produce physically unreliable predictions.

5.5. Engineering Implications

The proposed framework is useful for engineering applications where both axial and radial magnetic forces must be estimated efficiently. In electromagnetic actuators, radial force may introduce side loading, friction, vibration, or bearing stress. In wireless power transfer systems, misalignment can reduce coupling efficiency and create unwanted transverse forces. In calibration platforms, accurate force prediction is required for reliable reference loading. In superconducting or high-current coil systems, force distribution affects structural loading and mechanical design.

The framework provides several levels of model fidelity. The semi-analytical method is suitable for rapid early-stage coaxial design. The direct numerical method is useful for physics-based verification. The filament-based method is appropriate when practical winding details are important. Ansys Maxwell provides an independent finite-element software benchmark. The surrogate model enables fast repeated prediction and optimization within the validated training domain.

This multi-level structure allows the user to choose an appropriate balance among speed, physical detail, and validation rigor.

5.6. Limitations and Uncertainty

Several limitations define the scope of the present work. First, the study is limited to software-based validation against Ansys Maxwell. Physical experimental validation is not included. Real-world measurements may be affected by winding imperfections, fixture tolerances, current-source uncertainty, force-sensor calibration error, thermal expansion, and mechanical deformation.

Second, the formulation is magnetostatic. High-frequency effects such as skin effect, proximity effect, eddy-current redistribution, displacement current, radiation, and frequency-dependent current distribution are not included. These effects may become important in high-frequency wireless power transfer, pulsed actuators, and rapidly switched electromagnetic systems.

Third, the analytical and filament-based models assume an air-core medium with $\mu_r = 1$. Ferromagnetic cores, magnetic shielding, nonlinear permeability, saturation, hysteresis, and nearby conductive structures require additional finite-element or reduced-order material modeling.

Fourth, the current distribution is prescribed. Thermal variation, conductor deformation, current redistribution, and coupling between electromagnetic and mechanical deformation are not included.

Fifth, the validation is based on a selected baseline coil family. Although the surrogate dataset includes variations in geometry, current, offset, tilt, pitch, and conductor diameter, additional coil families should be studied to further test generality.

Finally, the surrogate model is valid only inside the sampled training range. It should not be used for extrapolation without additional validated data or retraining.

5.7. Future Work

Future work should focus on physical experimental validation. A suitable validation platform should include real air-core coil pairs, calibrated force sensors, controlled DC current excitation, precision current measurement, axial and lateral translation stages, tilt-control fixtures, and nonmagnetic mechanical supports. Measurements should include axial-force sweeps, lateral-offset radial-force tests, angular-tilt tests, current-scaling tests, and practical winding-effect comparisons.

Further computational extensions should include AC excitation, eddy-current effects, skin and proximity effects, magnetic-material coupling, ferromagnetic-core systems, thermal effects, mechanical deformation, and measured-winding geometry. The surrogate model can also be improved by adding more coil geometries, larger misalignment ranges, physics-informed constraints, and future experimental data.

5.8. Summary of Discussion

The discussion confirms that the proposed framework successfully extends ideal coaxial coil-force analysis to practical air-core coil systems with axial and radial force prediction. The software-validation results show stable Ansys Maxwell reference behavior, strong agreement among physics-based methods, accurate radial-force symmetry, reliable angular-misalignment prediction, and clear improvement when practical winding details are included.

The most important numerical findings are as follows: the mesh-independence change is 0.15%; the boundary-domain sensitivity is 0.12%; the maximum physics-based half-spread is 0.55%; the maximum axial-force deviation is 0.62%; the radial-force sign-symmetry error is 0.23%; and the practical winding model reduces vector error from 2.87% to 0.10%. The surrogate model achieves $R^2 = 0.9960.998$, mean relative error below 1.20%, and maximum relative error of 5.00%.

Overall, the framework provides a reliable and efficient tool for software-validated axial and radial magnetic-force prediction in practical misaligned air-core coil systems. It is suitable for preliminary design, numerical verification, misalignment analysis, winding-effect evaluation, and surrogate-assisted optimization, while physical experimental validation remains a necessary future step.

6. CONCLUSION

This paper has presented a software-validated computational framework for predicting axial and radial magnetic forces in practical air-core coil systems under aligned and misaligned conditions. The framework extends ideal coaxial coil-force analysis by incorporating finite coil dimensions, lateral offset, angular tilt, radial and tangential force components, discrete winding geometry, helical winding pitch, finite conductor diameter, and nonuniform conductor placement. Three complementary physics-based methods were implemented: a semi-analytical elliptic-integral method, a direct numerical-integration method based on the Lorentz-force interaction integral, and a filament-based discrete-winding method for practical conductor geometry. A feedforward neural-network surrogate model was also developed for rapid force prediction within the validated parameter domain.

Independent Ansys Maxwell simulations were used as the finite-element software-validation reference. The software reference solution was verified through mesh-independence and boundary-domain sensitivity tests. The final mesh-independence change was 0.15%, and the final boundary-domain sensitivity was 0.12%, confirming that the finite-element reference solution was sufficiently stable for model comparison. This work is limited to software-based validation; physical experimental validation is not claimed and is identified as future work.

The validation results show strong agreement among the proposed methods and Ansys Maxwell reference simulations. For the coaxial axial-force sweep, the maximum relative deviation among the semi-analytical, direct numerical, filament-based, Ansys Maxwell, and surrogate predictions was 0.62%. For laterally offset coils, the radial force was zero under perfect alignment and changed sign when the offset direction was reversed, with a maximum sign-symmetry error of 0.23%. For angular and combined offset-and-tilt cases, the maximum vector-force error was 0.42%, confirming that the framework can evaluate general non-coaxial force behavior.

The comparison among physics-based methods further confirmed the internal consistency of the framework. The maximum relative half-spread among the semi-analytical, direct numerical, and filament-based predictions was 0.55%. The direct numerical and filament-based convergence tests both showed final refinement changes of 0.09%. The current-scaling verification produced a maximum error of 0.77%, confirming that the current magnitude, current direction, and force sign convention were implemented consistently.

The practical winding comparison showed that winding representation has a measurable effect on prediction accuracy. The model-to-software vector error decreased from 2.87% for the continuous-current approximation to 0.10% for the full practical winding model. This confirms that discrete turns, helical pitch, finite conductor diameter, and realistic conductor placement improve agreement with finite-element simulation. Although the baseline helical pitch angle is small, approximately 0.211°, the helical representation improves agreement because it better matches the actual conductor path and winding geometry.

The surrogate model provided accurate and computationally efficient prediction within the sampled design domain. Using 12000 validated samples, the surrogate achieved $R^2 = 0.9960.998$, mean relative error below 1.20%, and maximum relative error of 5.00% on unseen test data. The surrogate is suitable for rapid interpolation, parametric studies, and optimization within the validated training range. It should not be used for extrapolation outside the sampled parameter space without additional validated data or retraining.

Overall, the proposed framework provides a reliable and physically interpretable tool for axial and radial magnetic-force prediction in practical air-core coil systems. It supports preliminary actuator design, wireless power transfer alignment analysis, inductive coupling studies, magnetic calibration systems, numerical solver verification, winding-effect evaluation, and surrogate-assisted optimization. Future work will focus on physical experimental validation using real air-core coil pairs, calibrated force sensors, controlled current excitation, axial and lateral translation stages, and tilt-control fixtures. Additional extensions should include AC excitation, eddy-current effects, skin and proximity effects, magnetic-material coupling, thermal deformation, mechanical deformation, and physics-informed surrogate modeling.

REFERENCES

[1] Grover, F. W., *Inductance Calculations: Working Formulas and Tables*, Dover Publications, New York, NY, USA, 2004.

[2] Babic, S. I. and C. Akyel, "Calculating mutual inductance between circular coils with inclined axes in air," *IEEE Transactions on Magnetics*, Vol. 44, No. 7, 1743–1750, 2008.

[3] Rosa, E. B., "The self and mutual inductances of linear conductors," *Bulletin of the Bureau of Standards*, Vol. 4, No. 2, 301–344, 1908.

[4] Kirsch, A. and F. Hettlich, *The Mathematical Theory of Time-harmonic Maxwell's Equations: Expansion, Integral, and Variational Methods*, Springer, Cham, Switzerland, 2016.

[5] Sondhi, K., N. Garraud, D. Alabi, D. P. Arnold, A. Garraud, S. G. R. Avuthu, Z. H. Fan, and T. Nishida, "Flexible screen-printed coils for wireless power transfer using low-frequency magnetic fields," *Journal of Micromechanics and Microengineering*, Vol. 29, No. 8, 084006, 2019.

[6] Xu, X., Z. Huang, W. Li, F. Dong, L. Hao, B. Shen, and Z. Jin, "Study on reducing the maximum perpendicular magnetic field of HTS coils used on synchronous generator armatures," *IEEE Transactions on Applied Superconductivity*, Vol. 29, No. 5, 1–5, 2019.

[7] Pankrac, V., "The algorithm for calculation of the self and mutual inductance of thin-walled air coils of general shape with parallel axes," *IEEE Transactions on Magnetics*, Vol. 48, No. 5, 1875–1889, 2012.

[8] Lemarquand, G., V. Lemarquand, S. Babic, and C. Akyel, "Magnetic field created by thin wall solenoids and axially magnetized cylindrical permanent magnets," in *PIERS Proceedings*, 614–618, Moscow, Russia, Aug. 2009.

[9] Braneshi, M., O. Zavalani, and A. Pijetri, "Evaluation of axial force between two coaxial disk coils," in *Proceedings of the 3rd International PhD Seminar on Computational Electromagnetics*, Ghent, Belgium, 2006.

[10] Ravaud, R., G. Lemarquand, S. Babic, V. Lemarquand, and C. Akyel, "Cylindrical magnets and coils: Fields, forces, and inductances," *IEEE Transactions on Magnetics*, Vol. 46, No. 9, 3585–3590, 2010.

[11] Maxwell, J. C., *A Treatise on Electricity and Magnetism*, Clarendon Press, Oxford, U.K., 1873.

[12] Abramowitz, M. and I. A. Stegun, *Handbook of Mathematical Functions*, Dover Publications, New York, NY, USA, 1965.

[13] Conway, J. T., "Exact solutions for the mutual inductance of circular coils and elliptic coils," *IEEE Transactions on Magnetics*, Vol. 48, No. 1, 81–94, 2012.

[14] Palka, R., "Fast analytic-numerical algorithms for calculating mutual and self-inductances of air coils," *Energies*, Vol. 17, No. 2, 325, 2024.

[15] Babic, S., E. Guven, K.-H. Song, and Y. Luo, "Optimized calculation of radial and axial magnetic forces between two non-coaxial coils of rectangular cross-section with parallel axes," *Computation*, Vol. 12, No. 9, 180, 2024.

[16] Wang, Y., X. Xie, and H. Wang, "Spatial magnetic field calculations for coreless circular coils with rectangular cross-section of arbitrary turn numbers," *Progress In Electromagnetics Research M*, Vol. 101, 9–23, 2021.

[17] Giovannetti, G., N. Fontana, A. Flori, M. F. Santarelli, M. Tucci, V. Positano, S. Barmada, and F. Frijia, "Machine learning for the design and the simulation of radiofrequency magnetic resonance coils: Literature review, challenges, and perspectives," *Sensors*, Vol. 24, No. 6, 1954, 2024.

[18] Barmada, S., N. Fontana, L. Sani, D. Thomopulos, and M. Tucci, "Deep learning and reduced models for fast optimization in electromagnetics," *IEEE Transactions on Magnetics*, Vol. 56, No. 3, 1–4, 2020.

[19] Landreman, M., S. Hurwitz, and T. M. Antonsen, "Efficient calculation of self magnetic field, self-force, and self-inductance for electromagnetic coils with rectangular cross-section," *Nuclear Fusion*, Vol. 65, No. 3, 036008, 2025.

[20] Yang, Y., W. S. P. Robertson, A. Jafari, and M. Arjomandi, "Optimising coil design based on sensitivity analysis of magnetic force induced between misaligned coil pairs," *Electrical Engineering*, Vol. 107, No. 12, 15 317–15 328, 2025.

[21] Khan, A., V. Ghorbanian, and D. Lowther, "Deep learning for magnetic field estimation," *IEEE Transactions on Magnetics*, Vol. 55, No. 6, 1–4, 2019.

[22] Ansys, Inc., "Ansys maxwell user's guide," Ansys Electronics Desktop 2026 R1, Canonsburg, PA, USA, 2026.

[23] Jebelli, A., N. Lotfi, A. Mahabadi, and M. C. E. Yagoub, "Unified analytical and numerical evaluation of axial magnetic force in coaxial air-core coils," *Progress In Electromagnetics Research B*, Vol. 117, 135–149, 2026.

[24] Jebelli, A., A. Mahabadi, H. Chaoui, and M. C. E. Yagoub, "Simulation of magnetic force between two coaxial coils with air core and uniform flow in MATLAB," *International Journal of Physics*, Vol. 9, No. 4, 186–196, 2021.

[25] Jebelli, A., A. Mahabadi, M. C. E. Yagoub, and H. Chaoui, "Magnetic force calculation between magnets and coils," *International Journal of Physics*, Vol. 8, No. 2, 71–80, 2020.